

# SPECTRAL METHODS FOR TIME-DEPENDENT STUDIES OF ACCRETION FLOWS. I. TWO-DIMENSIONAL, VISCOUS, HYDRODYNAMIC DISKS

CHI-KWAN CHAN, DIMITRIOS PSALTIS, AND FERYAL ÖZEL<sup>1</sup>

Physics and Astronomy Departments, University of Arizona, 1118 E. 4th St., Tucson, AZ 85721

*Draft version November 1, 2018*

## ABSTRACT

We present a numerical method for studying the normal modes of accretion flows around black holes. In this first paper, we focus on two-dimensional, viscous, hydrodynamic disks, for which the linear modes have been calculated analytically in previous investigations. We use pseudo-spectral methods and low storage Runge-Kutta methods to solve the continuity equation, the Navier-Stokes equation, and the energy equation. We devise a number of test problems to verify the implementation. These tests demonstrate the ability of spectral methods to handle accurately advection problems and to reproduce correctly the stability criteria for differentially rotating hydrodynamic flows. They also show that our implementation is able to handle sound wave correctly with non-reflective boundary conditions, to recover the standard solution for a viscous spreading ring, and produce correctly the Shakura-Sunyaev steady disk solution. Finally, we have applied our algorithm to the problem of a non-axisymmetric viscous spreading ring and verify that such configuration is unstable to non-antisymmetric perturbations.

*Subject headings:* accretion disks, black hole physics, hydrodynamics

## 1. INTRODUCTION

Observations of accretion flows around black holes in galactic systems and in the centers of galaxies show strong evidence for the presence of long-lived, global modes at characteristic frequencies of the black-hole spacetimes (see van der Klis 2000; McClintock, & Remillard 2004, for reviews). The origin of these modes is still a matter of debate (see, e.g., Psaltis 2001, 2004). It is anticipated, however, that modeling accurately their origin and physical properties will provide the first measurements of the spins of black holes in the universe as well as direct tests of strong-field general relativity (Psaltis 2004).

Systematic studies of modes in accretion disks around black holes have so far been mostly analytical, performed in the linear regime for flows with an artificial viscosity law (see Wagoner 1999; Kato 2001, and reference therein; see, however, Gammie & Balbus 1994 and Menou 2003 for studies of MHD disks). These studies have shown the presence of three types of trapped global modes, namely inertial-gravity, corrugation, and inertial-pressure modes, with properties that appear to agree with observations (see Wagoner et al. 2001).

Despite their success, analytical models have several limitations. First, they rely on a number of approximations, such as the WKB approximation in the radial direction. Second, because only linear terms in perturbations are taken into account, these studies are unable to reproduce resonances and couplings between various modes. However, the detected QPOs often have fractional amplitudes as large as 40% of the total X-ray flux, making the linear approximation inaccurate (see, e.g., McClintock, & Remillard 2004). Furthermore, pairs of QPOs are typically observed (see Strohmayer 2001a,b) with frequency ratios equal to ratios of small integers, strongly arguing for the presence of resonances between modes (Abramowicz, & Kluźniak 2001). Third, analytical and numerical studies of oscillations in MHD disks cast doubt on the presence of oscillations at the radial epicyclic frequencies, as required by all diskoseismic calculations (see, e.g.,

Hawley, & Krolik 2001, 2002; Armitage, & Reynolds 2003). Answering all the above questions necessitates a systematic, numerical study of accretion disk oscillations.

Numerical studies of accretion disk modes have been very few and have not addressed in detail the above issues (see, e.g., Chen, & Taam 1994, 1995; Milsom, & Taam 1996, 1997, for simulations of viscous disks; see also Rezzolla 2004 for simulations of hydrodynamic tori). In fact, no numerical simulation of hydrodynamic disks to date has resulted in solutions that show all three types of accretion-disk modes that were discovered analytically. In this series of papers, we perform a systematic study of the oscillatory behavior of hydrodynamic and MHD accretion disks in two and three dimensions. To this end, we have developed a pseudo-spectral numerical algorithm, which we present here. Even though spectral methods have been used extensively in the study of hydrodynamic modes in various planetary atmospheres, including the earth's (see, e.g., Mote, & O'Neill 2000), their application to the studies of accretion disks has been very limited (Godon 1997).

Spectral algorithms are high order numerical methods and are perfectly suited to studying modes of hydrodynamic flows for a number of reasons. Their major advantage is accuracy and economy in the number of degrees of freedom (Bonazzola et al. 1999). In spectral methods, only  $\sim \pi$  collocation points are needed to resolve one wavelength (Boyd 2000), whereas in finite difference methods a lot more grid points are required to reach the same accuracy. The solution is already expressed as a set of orthogonal modes; this property improves the accuracy of studies of mode coupling and resonance. Moreover, the dimensionality of the problem can be altered very easily, for investigating the effects of the number of spatial dimensions on the properties of hydrodynamic modes and turbulence. In simulating MHD flows, the high order of spectral methods allows for the equations to be solved in terms of the vector potential and not of the magnetic field itself; this guarantees that the resulting magnetic field is always divergence free. Also, super spectral viscosity (Ma 1998a,b), which is one kind of artificial viscosity, is trivial to implement

<sup>1</sup> Hubble Fellow

in spectral methods. It resolves shocks and yet preserves the high spectral accuracy of the solution. Finally, incorporating the self-gravity of the flows is trivial and does not increase significantly the computational time (see, e.g., Chen et al. 2000).

In this first paper, we discuss our numerical algorithm for evolving two-dimensional viscous, hydrodynamic accretion disks. In the following section, we present our assumptions and equations. In §3, we discuss the details of our numerical method. In §4, we present a series of tests to verify our algorithm. In §5, we apply our algorithm to non-axisymmetric instabilities in viscous spreading rings. We confirm the result of Speith, & Kley (2003), which shows that the standard solution of a viscous spreading ring (Pringle 1981; Frank, King, & Raine 2002) is unstable to non-axisymmetric perturbation. In §6, we present our conclusions.

## 2. EQUATIONS AND ASSUMPTIONS

We consider two-dimensional, viscous, compressible flows. In this first paper, we neglect self-gravity and the magnetic fields of the flows. The hydrodynamic equations, therefore, contain the continuity equation

$$\frac{\partial \Sigma}{\partial t} + \nabla \cdot (\Sigma \mathbf{v}) = 0, \quad (1)$$

the Navier-Stokes equation

$$\Sigma \frac{\partial \mathbf{v}}{\partial t} + \Sigma (\mathbf{v} \cdot \nabla) \mathbf{v} = -\nabla P + \nabla \tau - \Sigma \mathbf{g}, \quad (2)$$

and the energy equation

$$\frac{\partial E}{\partial t} + \nabla \cdot (E \mathbf{v}) = -P \nabla \cdot \mathbf{v} + \Phi - \nabla \cdot \mathbf{q} - \nabla \cdot \mathbf{F} - 2F_z. \quad (3)$$

We denote by  $\Sigma$  the height-integrated density, by  $\mathbf{v}$  the velocity, and by  $E$  the thermal energy. In the Navier-Stokes equation,  $P$  is the height-integrated pressure,  $\tau$  is the viscosity tensor, and  $\mathbf{g}$  is the gravitational acceleration. We use  $\Phi$  to denote the viscous dissipation rate,  $\mathbf{q}$  to denote the heat flux vector, and  $\mathbf{F}$  to denote the radiation flux on the  $r$ - $\phi$  plane. The last term in the heat equation,  $2F_z$ , takes into account the radiation losses in the vertical direction.

We allow for large flexibility in the physical assumptions in our algorithm, i.e., we can change the functional form of  $P$ ,  $\mathbf{g}$ ,  $\mathbf{q}$ ,  $\mathbf{F}$ , and  $F_z$  easily and apply our algorithm to various problems. We also write the viscosity tensor in the general form

$$\tau_{ij} = 2(\mu_r + \mu_s)e_{ij} + \left( \mu_r + \mu_b - \frac{2}{3}\mu_s \right) \nabla \cdot \mathbf{v}. \quad (4)$$

Here  $\mu_r$ ,  $\mu_b$ , and  $\mu_s$  are the coefficients of radiative, bulk, and shear viscosity, respectively. These coefficients can also be changed easily to satisfy different physical assumptions. The strain-rate tensor  $e_{ij}$  is

$$e_{ij} = \frac{1}{2} \left( \frac{\partial v_i}{\partial x_j} + \frac{\partial v_j}{\partial x_i} \right). \quad (5)$$

The viscous dissipation rate is

$$\Phi = 2(\mu_r + \mu_s)(e_{ij})^2 + \left( \mu_r + \mu_b - \frac{2}{3}\mu_s \right) (\nabla \cdot \mathbf{v})^2. \quad (6)$$

In appendix A, we write down explicitly the equations used in the algorithm.

The default setup for our calculations is that of a geometrically thin disk, in which radiation pressure is assumed to be

negligible. Using the ideal gas law, the thermal energy density and pressure become

$$E = \Sigma \frac{3k_B T}{2\mu m_H}, \quad (7)$$

$$P = \Sigma \frac{k_B T}{\mu m_H}, \quad (8)$$

where  $k_B$  is the Boltzmann constant,  $T$  is the central temperature,  $\mu$  is the mean molecular weight, and  $m_H$  is the mass of the hydrogen atom. The viscosity coefficients  $\mu_r$ ,  $\mu_b$ , and  $\mu_s$  are chosen based on the physical assumptions of the specific problems.

In order to approximate the effects of general relativity in the vicinity of compact objects, we use the pseudo-Newtonian approximation for the gravitational acceleration (Paczynsky, & Wiita 1980; Mukhopadhyay 2002)

$$\mathbf{g} = \frac{c^2}{r^3} \left[ \frac{GM}{c^2} \right]^2 \left[ \frac{r^2 - 2(a/c)\sqrt{GM/c^2} + (a/c)^2}{\sqrt{GM/c^2}(r - r_g) + a/c} \right]^2 \hat{\mathbf{r}}. \quad (9)$$

Here,  $c$  is speed of light,  $G$  is the gravitational constant,  $M$  is the mass of the central object,  $a$  is its specific angular momentum,  $r_g = 2GM/c^2$  is its Schwarzschild radius, and  $\hat{\mathbf{r}}$  is the unit vector in the radial direction. For a non-rotating star, we set  $a = 0$  and the gravitational acceleration reduces to the standard pseudo-Newtonian acceleration  $g = GM/(r - r_g)^2$ . When  $a = r_g = 0$ , it recovers Newtonian gravity.

Regarding radiative cooling, we follow Hubeny (1990) and Popham, & Narayan (1995) to take into account the energy loss in the vertical direction by the standard form

$$F_z = \frac{4\sigma_{\text{SB}} T^4}{3\tau_d}, \quad (10)$$

where we use  $\sigma_{\text{SB}}$  to denote the Stefan-Boltzmann constant. The optical depth  $\tau_d$  is again chosen based on the physical problem. We finally set to zero the other two terms,  $\nabla \cdot \mathbf{q}$  and  $\nabla \cdot \mathbf{F}$ , in the energy equation.

## 3. NUMERICAL METHOD

In our numerical algorithm, we use pseudo-spectral methods to evaluate the spatial derivatives in the partial differential equations and an explicit Runge-Kutta method to advance the solution in time.

Spectral methods are based on the idea that any function can be expanded in a series of orthogonal basis functions. When a well-behaved basis is chosen, this series converges exponentially in the absence of discontinuities and the numerical partial derivatives can be easily evaluated. There exist different ways to approximate functions by a series with a finite number of terms, such as the Galerkin method, the tau method, and the pseudo-spectral method (see Canuto 1988; Gottlieb, & Orszag 1983; Guo 1998; Boyd 2000; Peyret 2002). In pseudo-spectral methods, as the one we use here, we choose a set of collocation points and then evaluate the expansion (spectral) coefficients such that the truncated series agree exactly with the original functions at the collocation points up to the machine accuracy. In the next subsection, we discuss our implementation of the pseudo-spectral method.

### 3.1. Collocation Methods

The Fourier basis is the natural choice for expanding functions with periodic boundary conditions, as is the case along

the azimuthal direction in our problem. Any physical quantity  $f = f(r, \phi)$  can be expanded in this basis as

$$f(r, \phi) = \sum_{m=-\infty}^{\infty} \hat{f}_m(r) e^{im\phi}. \quad (11)$$

We use a total of  $M$  evenly spaced, discrete collocation points in the domain  $[-\pi, \pi)$ ,

$$\phi_j \equiv \frac{2\pi j}{M}, \quad \text{for } -\frac{M}{2} \leq j \leq \frac{M}{2} - 1, \quad (12)$$

so that the above Fourier series can be approximated by the (truncated) discrete Fourier series

$$f(r, \phi_j) = \sum_{m=-M/2}^{M/2-1} \hat{f}_m(r) e^{i2\pi mj/M}. \quad (13)$$

The derivative of  $f$  with respect to  $\phi$  is, therefore,

$$\left. \frac{\partial f}{\partial \phi} \right|_{\phi_j} = \sum_{m=-M/2}^{M/2-1} im \hat{f}_m(r) e^{i2\pi mj/M}. \quad (14)$$

In order to evaluate equation (14), we use a fast Fourier transform algorithm to find  $\hat{f}_m$ , multiply the Fourier coefficients by  $im$ , and then take the inverse fast Fourier transform of the series. The computational order of the azimuthal derivative is therefore  $\mathcal{O}(M \log_2 M)$ .

When non-periodic boundary conditions are present, as in the case along the radial direction, the Fourier basis can no longer be used. Popular choices of bases are the Legendre and Chebyshev polynomials, which are both defined on the domain  $[-1, 1]$ . Between these two, the Chebyshev polynomials are usually preferred because of their relation to the cosine function, which makes them easier to compute. Suppose the domain of  $r$  is  $[r_{\min}, r_{\max}]$ . In order to map the standardized radial coordinate  $\bar{r} \in [-1, 1]$  to the physical radial coordinate  $r \in [r_{\min}, r_{\max}]$ , we introduce a mapping function  $r = g(\bar{r})$  which is strictly increasing and satisfies both  $g(-1) = r_{\min}$  and  $g(1) = r_{\max}$ . Let  $T_n(\bar{r})$  be the  $n$ -th order Chebyshev polynomial, i.e.,

$$T_n(\bar{r}) \equiv \cos(n \arccos \bar{r}). \quad (15)$$

The Chebyshev-Gauss-Lobatto collocation points are defined by

$$\bar{r}_k \equiv \cos\left(\frac{\pi k}{N}\right), \quad \text{for } 0 \leq k \leq N, \quad (16)$$

where the collocation points in the physical radial coordinate are given by  $r_k = g(\bar{r}_k)$ . Note that there are totally  $N+1$  collocation points including both boundary points of the domain. For any physical quantity  $f(r, \phi)$ , we approximate its Chebyshev-Fourier series by the double sum

$$\begin{aligned} f(r_k, \phi_j) &= f[g(\bar{r}_k), \phi_j] \\ &= \sum_{m=-M/2}^{M/2-1} \sum_{n=0}^N \tilde{f}_{n,m} T_n(\bar{r}_k) e^{i2\pi mj/M} \\ &= \sum_{m=-M/2}^{M/2-1} \sum_{n=0}^N \tilde{f}_{n,m} \cos\left(\frac{\pi nk}{N}\right) e^{i2\pi mj/M}. \end{aligned} \quad (17)$$

We then use a fast discrete cosine transform to obtain the spectral coefficient  $\tilde{f}_{n,m}$  from  $\hat{f}_m(r) = \hat{f}_m[g(\bar{r})]$ . The radial derivative can be found using the chain rule

$$\frac{\partial f}{\partial r} = \frac{1}{dg/d\bar{r}} \frac{\partial f}{\partial \bar{r}}. \quad (18)$$

Expressing the derivative with respect to the standardized coordinate as

$$\frac{\partial f}{\partial \bar{r}} = \sum_{m=-M/2}^{M/2-1} \sum_{n=0}^N \tilde{f}_{n,m}^{(1)} T_n(\bar{r}) e^{im\phi}, \quad (19)$$

we can employ the following three-term recursive relation to obtain  $\tilde{f}_{n,m}^{(1)}$  from  $\tilde{f}_{n,m}$ ,

$$\begin{cases} \tilde{f}_{N,m}^{(1)} = 0, \\ \tilde{f}_{N-1,m}^{(1)} = 2N \tilde{f}_{N,m}, \\ c_n \tilde{f}_{n,m}^{(1)} = \tilde{f}_{n+2,m}^{(1)} + 2(n+1) \tilde{f}_{n+1,m}, \end{cases} \quad (20)$$

where  $c_0 = 2$ , and  $c_n = 1$ , for  $n > 1$ . This recursion relation allows the use of an  $\mathcal{O}(N)$  algorithm in calculating the numerical derivatives in spectral space along the radial direction. The transformation between physical and spectral space can then be done by a fast cosine transform, the order of which is  $\mathcal{O}(N \log_2 N)$ .

The most trivial map  $r = g(\bar{r})$  is linear, i.e.,

$$r = \frac{r_{\max}}{2}(\bar{r} + 1) - \frac{r_{\min}}{2}(\bar{r} - 1). \quad (21)$$

In this case,

$$\frac{1}{dg/d\bar{r}} = \frac{d\bar{r}}{dr} = \frac{2}{r_{\max} - r_{\min}} \quad (22)$$

is just a constant. However, the grid spacings  $\Delta r_k = r_k - r_{k-1}$ , for  $1 \leq k \leq N$ , scale with the number of collocation points  $N$  as  $\Delta r_k = \mathcal{O}(N^{-2})$ , when  $k$  is close to 1 or  $N$ . This requires the stability condition for time-stepping to be

$$\Delta t = \mathcal{O}(N^{-4}) \quad (23)$$

due to viscous time scale (see §3.6). The grid spacings for Fourier collocation are  $\Delta \phi_j = \phi_j - \phi_{j-1}$ . They are uniform and scale as  $\Delta \phi_j = \mathcal{O}(M^{-1})$  which gives the stability condition

$$\Delta t = \mathcal{O}(M^{-2}). \quad (24)$$

The stability condition in the radial direction is too expensive numerically compared to the one required by the azimuthal direction. To overcome this restriction, Kosloff, & Tal-Ezer (1993) proposed the mapping

$$r = \frac{r_{\max}}{2} \left[ \frac{\arcsin(\alpha \bar{r})}{\arcsin(\alpha)} + 1 \right] - \frac{r_{\min}}{2} \left[ \frac{\arcsin(\alpha \bar{r})}{\arcsin(\alpha)} - 1 \right], \quad (25)$$

which makes the spacing  $\Delta r_k = \mathcal{O}(N^{-1})$  around the boundaries. In the above transformation,  $\alpha$  is a parameter. Let  $\epsilon$  be the machine accuracy. Don, & Solomonoff (1997) showed that the choice

$$\alpha = \text{sech}\left(\frac{|\ln \epsilon|}{N}\right) \quad (26)$$

minimizes the errors in the numerical derivatives. We therefore refer to the mapping (25) with the optimized choice (26) as the modified Chebyshev collocation and employ it in our algorithm. The numerical derivatives for the modified Chebyshev collocation can be easily calculated by

$$\left. \frac{\partial f}{\partial r} \right|_{r_k} = \frac{2 \arcsin(\alpha)}{(r_{\max} - r_{\min}) \alpha} \sqrt{1 - (\alpha r_k)^2} \left. \frac{\partial f}{\partial \bar{r}} \right|_{\bar{r}_k}, \quad (27)$$

where  $(\partial f / \partial \bar{r})|_{\bar{r}_k}$  is obtained by the usual Chebyshev method (19). The constant scaling in (22) and the scaling in equation (27) can be done together with the normalization, so neither of them have extra computational cost.

### 3.2. Treatment of the Non-Linear Terms

In low order numerical methods, one uses the conservative form of the hydrodynamic equations to ensure conservation of mass and momentum (LeVeque 1992). This is not necessarily the ideal way for pseudo-spectral methods because the conservative form is sometime numerically unstable (see Peyret 2002, pp.286–289). To illustrate this, consider two arbitrary functions  $u(x)$  and  $v(x)$ . The derivative of their product has two different but equivalent forms

$$C = (uv)', \quad (28)$$

$$D = u'v + uv'. \quad (29)$$

The pseudo-spectral Fourier coefficients (with  $M$  collocation points) of  $C$  and  $D$  are

$$\hat{C}_m = im \sum_{p+q=m} \hat{u}_p \hat{v}_q + i \left[ \sum_{p+q=m+M} m \hat{u}_p \hat{v}_q + \sum_{p+q=m-M} m \hat{u}_p \hat{v}_q \right], \quad (30)$$

$$\hat{D}_m = im \sum_{p+q=m} \hat{u}_p \hat{v}_q + i \left[ \sum_{p+q=m+M} (m+M) \hat{u}_p \hat{v}_q + \sum_{p+q=m-M} (m-M) \hat{u}_p \hat{v}_q \right]. \quad (31)$$

The first term in each equation corresponds to the truncated Fourier series. The other terms in the square brackets are therefore due to the aliasing error of pseudo-spectral methods (see Boyd 2000, pp.202–221), which may cause numerical instability. One can show that these aliasing terms have opposite signs. The skew symmetric form  $(\hat{C}_m + \hat{D}_m)/2$ , therefore, has a much smaller aliasing error. Unfortunately, calculating the skew symmetric form increases the number of numerical derivatives and lowers the algorithmic performance.

A similar argument is valid for the Chebyshev collocation. However, in that case, the problem becomes more complicated due to the boundary conditions. Botella, & Peyret (2001) carried out numerical experiments and reported that, without aliasing removal, the convective form is stable for the two different boundary method they tested; the conservative form is unstable for one of their methods. We carried out some numerical experiments for our algorithm. When the initial conditions are smooth, both conservative and convective forms are stable. However, when an initial perturbation is introduced, the conservative form sometimes become unstable. In these cases, the spectral coefficients at high wavenumbers in the radial direction grow exponentially even with spectral filtering (see the next subsection). The convective form, on the other hand, is able to reproduce various analytical stability criteria, as shown in §4.

Because the convective form gives an approximation that is of the same order as the conservative form, in the present implementations of the numerical algorithm, we use the convective form for the non-linear terms in Navier-Stokes equation to ensure numerical stability. The continuity and energy equations, on the other hand, are written in conservative form to conserve mass and energy. The exact equations we solve in the algorithm can be found in appendix A.

### 3.3. Spectral Filtering

In our numerical algorithm, we use a combination of spectral filters in order to resolve the two principle drawbacks of spectral methods. First, because of the non-linear character of the Navier-Stokes equations described above, we need to filter out the high-frequency modes in each time step to reduce the aliasing error. The spectral filters ensure long-time stability of the algorithm. Second, when shocks are present in the solutions, the spectral coefficients do not converge exponentially and oscillations appear around the discontinuities (Gibbs phenomenon). Introducing an additional spectral filter increases the converge rate of the solutions. Indeed, it has been proven that the filtered solution converges to the correct entry solution and hence gives the correct shock properties. (For more information see Don 1994; Don, & Quillen 1995; Gottlieb, & Shu 1997; Ma 1998a,b; Guo et al. 2001; Li 2001, and reference therein.)

Suppose we want to apply a filter in the  $\phi$ -direction. We first find the Fourier coefficients  $\hat{f}_m(r)$  according to equation (11). We then denote the filtered sum by

$$f^{\sigma_\beta}(r, \phi_j) = \sum_{m=-M/2}^{M/2-1} \sigma_\beta \left( \frac{2m}{M} \right) \hat{f}_m(r) e^{i2\pi m j/M}, \quad (32)$$

where we use the exponential filter

$$\sigma_\beta \left( \frac{2m}{M} \right) = \exp \left( -|\ln \epsilon| \left| \frac{2m}{M} \right|^\beta \right). \quad (33)$$

The parameter  $\epsilon$  here is again the machine accuracy. We choose  $\beta \approx M/2$  so that the filtered sum approximates the original function very well and does not reduce the accuracy of the numerical solution. The same filter is used in the radial direction, i.e.,

$$\sigma_\beta \left( \frac{n}{N} \right) = \exp \left( -|\ln \epsilon| \left| \frac{n}{N} \right|^\beta \right), \quad (34)$$

where  $\beta$  is chosen close to  $N$  so the double filtered sum is

$$f^{\sigma_N, \sigma_{M/2}}(r_k, \phi_j) = \sum_{m=-M/2}^{M/2-1} \sum_{n=0}^N \sigma_N \left( \frac{n}{N} \right) \sigma_{M/2} \left( \frac{2m}{M} \right) \times \check{f}_{n,m} \cos \left( \frac{\pi n k}{N} \right) e^{i2\pi m j/M}. \quad (35)$$

### 3.4. Initial Perturbations

Spectral methods have been used successfully to study non-randomized perturbation, such as the tidal effects presented by Godon (1997, 1998). Later, Godon, & Livio (2000) described a method to add random perturbations to their initial conditions. In their simulation, they generated 100 Gaussian profiles randomly within the computation domain. This method ensure that the spectral coefficients of the perturbed function converge exponentially, and avoids changing the direction of the characteristic at the boundary.

In our calculations, we require the initial perturbations to be smooth, i.e., we require the spectrum of the perturbations to converge exponentially. One simple method to obtain such a perturbation is to generate random noise in spectral space, multiply the noise by an exponential filter, and transform the noise back to physical space.

To formulate this method, we first generate a flat-noise spectrum,  $\check{P}_{n,m}$ , which is totally random. The perturbation is added to the original function by the following equation

$$f(r, \phi) = [1 + \gamma(r, \phi) P^{\sigma_\beta, \sigma_\beta}(r, \phi)] f_0(r, \phi), \quad (36)$$

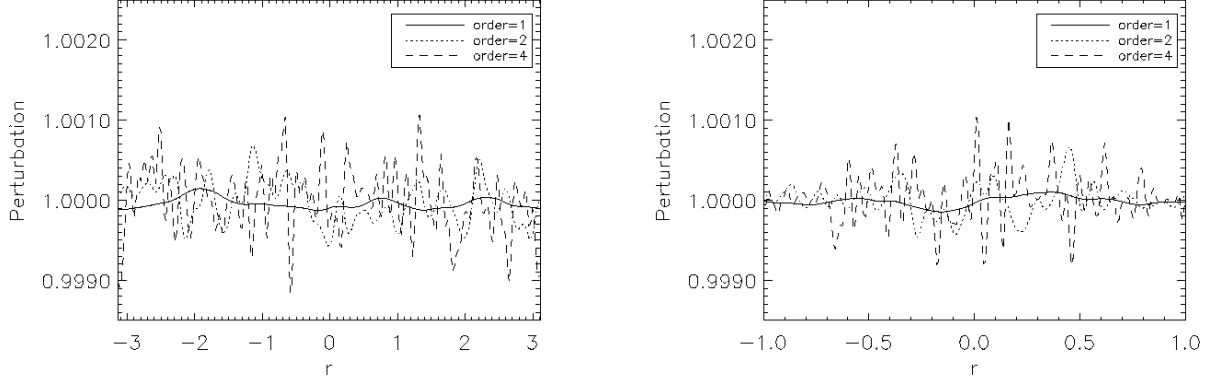


FIG. 1.— Two 1-dimension perturbation profiles generated by the method describe in §3.4. All lines in the plots have  $\gamma_0 = 0.001$ . (Left) The function is assumed periodic and approximated by a Fourier collocation. (Right) A Chebyshev collocation is used to demonstrate the behavior of our method near the boundaries.

where  $f(r, \phi)$  is the perturbed function,  $\gamma(r, \phi)$  is the size of the perturbation,  $P^{\sigma_\beta, \sigma_\beta}(r, \phi)$  is the filtered sum

$$P^{\sigma_\beta, \sigma_\beta}(r_k, \phi_j) = \sum_{m=-M/2}^{M/2-1} \sum_{n=0}^N \sigma_N \left( \frac{n}{\beta} \right) \sigma_{M/2} \left( \frac{m}{\beta} \right) \times \check{P}_{n,m} \cos \left( \frac{\pi n k}{N} \right) e^{i 2 \pi m j / M}, \quad (37)$$

as defined in the pervious subsection, and  $f_0(r, \phi)$  is the unperturbed function. The order of filter,  $\beta$ , controls the spacial scale of the perturbation. Because  $f_0(r, \phi)$  is periodic in  $\phi$ , we can simply use a  $\phi$ -independent function  $\gamma(r, \phi) = \gamma(r)$ . However, in the  $r$ -direction we do not want the perturbation to extend the boundaries. We, therefore, set

$$\gamma(r) = \gamma_0 \frac{\arcsin(\alpha)}{\alpha} \sqrt{1 - (\alpha r)^2}, \quad (38)$$

which is pre-computed by equation (27), when we use the modified Chebyshev collocation method.

In Figure 1, we illustrate this method of introducing perturbations to an one-dimensional constant function  $f_0 = 1$ . The left plot uses a Fourier basis with 256 collocation points. Where the right plot uses a Chebyshev basis with 257 collocation points. All the lines have  $\gamma_0 = 0.001$  but different orders  $\beta$ . Note that the extra rescaling for Chebyshev collocation lowers the amplitude of the perturbations around the boundaries.

### 3.5. Boundary Conditions

Solving partial differential equations in a finite domain usually requires Dirichlet or/and Neumann boundary conditions. When using finite difference methods, one can simply change the values of physical quantities at the boundary points to achieve Dirichlet boundary conditions. Alternatively, one can adjust the “ghost points” to achieve Neumann boundary conditions. Unfortunately, these methods do not generally work for spectral methods. Indeed, changing the boundary points (or ghost points) effectively introduces step functions. When discontinuities are present, the spectral coefficients do not converge exponentially and the spectral methods fail to produce stable solutions.

Perturbations around the boundaries can also change the characteristic directions of the flow. A naive Dirichlet or Neumann boundary treatment fails to take care of these oscillations between inflowing and outgoing characteristics. When

the inflowing boundary conditions are not given, or when the outgoing boundary conditions are not consistent with the solutions in the computation domain, the system of differential equations is ill-posed and the algorithm diverges. Although we generate the initial perturbations in a way that they are small around the boundaries (see the previous subsection), they can still propagate and reach the boundaries as time evolves.

In our numerical algorithm, we introduce a new boundary treatment in the radial direction, which is a spatial filter. This method forces each dynamic variable to approach smoothly to its boundary value so the characteristics directions at the boundaries are well-defined. This ensures that any instabilities of the solution are not due to boundary conditions. For example, consider a one-dimensional problem

$$\frac{\partial f(r, t)}{\partial t} = F[f(r, t)] \quad (39)$$

for any functional form  $F$ . If we want to apply a Dirichlet boundary condition at the outer boundary, we choose some smooth monotonic function  $h(r)$  such that  $h(r) \rightarrow 1$  for interior points of the computational domain and  $h(r) \rightarrow 0$  at the boundary. At each time step, we impose the boundary condition by the spatial filter

$$f_k^i \rightarrow (f_k^i - f_0) h(r_k) + f_0, \quad (40)$$

where  $f_k^i$  denotes the numerical approximation of our function at time  $i$  and radial collocation point  $k$ . This filter makes the function  $f$  approach its boundary value  $f_0$  and produces a numerical boundary layer. Rearranging, the above step is equivalent to setting

$$f_k^i \rightarrow f_k^i - [1 - h(r_k)](f_k^i - f_0). \quad (41)$$

Hence, it is equivalent to adding an extra source/sink term  $\dot{f}_s$  in the original equation

$$\frac{\partial f}{\partial t} = F[f] - \frac{1 - h(r)}{\Delta t} (f - f_0) \equiv F[f] + \dot{f}_s, \quad (42)$$

where  $\Delta t$  is the time step (see §3.6). Omitting  $F$  in the above equation, it becomes  $\partial f / \partial t \sim -(f - f_0)$ . The value of  $[1 - h(r)] / \Delta t$  controls the converge rate of  $f$  to  $f_0$ , which is automatically proportional to the velocity, because  $1 / \Delta t \sim |\mathbf{v}|$ .

We use an exponential filter that is similar to the spectral filter discussed in §3.3. To impose an outer boundary condition, we need the monotonically decreasing filter

$$h(r) = \sigma_\beta \left( \frac{r - r_{\min}}{r_{\max} - r_{\min}} \right) = \exp \left[ -|\ln \epsilon| \left( \frac{r - r_{\min}}{r_{\max} - r_{\min}} \right)^\beta \right]. \quad (43)$$

On the other hand, for the inner boundary, we use the monotonically increasing filter

$$h(r) = \sigma_\beta \left( \frac{r_{\max} - r}{r_{\max} - r_{\min}} \right) = \exp \left[ -|\ln \epsilon| \left( \frac{r_{\max} - r}{r_{\max} - r_{\min}} \right)^\beta \right]. \quad (44)$$

We can change the thickness of the numerical boundary layer by changing the order of the filter,  $\beta$ .

This boundary treatment turns out to be very convenient in modeling non-reflective boundary conditions. When we choose the parameter  $\beta$  to be equal to the number of collocation points, the boundary layer is thick enough to discard any outgoing waves but thin enough so that the interior solution is not affected significantly.

For applying Neumann boundary conditions, the addition of a ghost zone is not practical in spectral methods. This is because Chebyshev polynomials approximate the derivatives based on all the interior points. Godon (1997) presented a method which involves solving for the boundary values of physical quantities, so that their derivatives agree with the boundary conditions. This is effectively a Dirichlet boundary treatment with the boundary values depending on all the interior values at each time step.

To avoid numerical instabilities due to the Neumann boundary conditions,  $(\partial f / \partial r)|_{\text{boundary}} = f'_0$ , we choose another method that involves applying a spatial filter to each variable after taking the radial derivatives. This is equivalent to replacing the radial derivatives  $(\partial f / \partial r)|_{r_k}$  by

$$\left. \frac{\partial f}{\partial r} \right|_{r_k}^i \rightarrow \left. \frac{\partial f}{\partial r} \right|_{r_k}^i - \left[ 1 - \sigma_\beta \left( \frac{r_k - r_{\min}}{r_{\max} - r_{\min}} \right) \right] \left( \left. \frac{\partial f}{\partial r} \right|_{r_k}^i - f'_0 \right) \quad (45)$$

for the inner boundary, and

$$\left. \frac{\partial f}{\partial r} \right|_{r_k}^i \rightarrow \left. \frac{\partial f}{\partial r} \right|_{r_k}^i - \left[ 1 - \sigma_\beta \left( \frac{r_{\max} - r_k}{r_{\max} - r_{\min}} \right) \right] \left( \left. \frac{\partial f}{\partial r} \right|_{r_k}^i - f'_0 \right) \quad (46)$$

for the outer boundary. This ensures that the first derivatives around the boundaries are smooth.

### 3.6. Time Stepping

We integrate the hydrodynamics equations with low-storage, explicit Runge-Kutta methods. Let

$$\mathbf{H} \equiv (H_\Sigma, H_{v_r}, H_{v_\phi}, H_E)^t \quad (47)$$

be the right hand sides of hydrodynamic equations (A1) – (A4) and let

$$\mathbf{u} \equiv (\Sigma, v_r, v_\phi, E)^t \quad (48)$$

be the dynamic variable; the superscript  $t$  here stands for transpose. The low-storage explicit Runge-Kutta methods have the general form

$$\begin{cases} \mathbf{u}_0 = \mathbf{u}(t_n) \\ \mathbf{Q}_i = A_i \mathbf{Q}_{i-1} + \Delta t \mathbf{H}(\mathbf{u}_{i-1}) \\ \mathbf{u}_i = \mathbf{u}_{i-1} + B_i \mathbf{Q}_i, \quad i = 1, \dots, s \\ \mathbf{u}(t_{n+1}) = \mathbf{u}_s \end{cases} \quad (49)$$

where  $\Delta t$  is the time step and  $A_1 = 0$ . All other  $A_i$ 's and  $B_i$ 's are coefficients that characterize the scheme and  $\mathbf{u}_i$  are the intermediate stages of  $\mathbf{u}$ . The method to obtain these coefficients can be found in Peyret (2002). Depending on the complexity of the problem, we choose between second order or third order Runge-Kutta, and third order or fourth order Carpenter-Kennedy Runge-Kutta methods. The different algorithms are compared during the verification tests (see §4.1 and fig. 3 below). The third order Runge-Kutta scheme, proposed by Williamson (See Peyret 2002, p.146), turns out to be the most popular in spectral methods because of its efficiency and accuracy. For this reason, we present here this scheme explicitly:

$$\begin{cases} \mathbf{u}_0 = \mathbf{u}(t_n) \\ \mathbf{Q}_1 = \Delta t \mathbf{H}(\mathbf{u}_0) \\ \mathbf{u}_1 = \mathbf{u}_0 + \frac{1}{3} \mathbf{Q}_1 \\ \mathbf{Q}_2 = -\frac{5}{9} \mathbf{Q}_1 + \Delta t \mathbf{H}(\mathbf{u}_1) \\ \mathbf{u}_2 = \mathbf{u}_1 + \frac{15}{16} \mathbf{Q}_2 \\ \mathbf{Q}_3 = -\frac{153}{128} \mathbf{Q}_2 + \Delta t \mathbf{H}(\mathbf{u}_2) \\ \mathbf{u}_3 = \mathbf{u}_2 + \frac{8}{15} \mathbf{Q}_3 \\ \mathbf{u}(t_{n+1}) = \mathbf{u}_3. \end{cases} \quad (50)$$

Recalling the definition of  $\Delta r_k$  and  $\Delta \phi_j$  in §3.1, we define the Courant-Friedrich-Lewy (CFL) time step in different directions independently,

$$\Delta t_{\text{CFL},r} = \min \left( \frac{\Delta r_k}{c_s + v_r} \right), \quad \Delta t_{\text{CFL},\phi} = \min \left( \frac{r_k \Delta \phi}{c_s + v_\phi} \right), \quad (51)$$

where  $c_s = \sqrt{P/\Sigma}$  is the sound speed. Let  $\Delta l \equiv \min(\Delta r_k, r_k \Delta \phi_j)$  be the minimum grid separation. We also define the viscously restricted time step as

$$\Delta t_{\nu_s} = \min \left( \frac{\Delta l^2}{\nu_s} \right), \quad (52)$$

where  $\nu_s = \mu_s / \Sigma$  is the kinematic viscosity coefficient. Using these definitions, the maximum allowed time step  $\Delta t$  is chosen adaptively by

$$\Delta t = \delta \min(\Delta t_{\text{CFL},r}, \Delta t_{\text{CFL},\phi}, \Delta t_{\nu_s}). \quad (53)$$

Here  $\delta$  is a constant that depends on the physical problem. For example, for a free falling dust ring, the flow is very stable and  $\delta$  could be chosen as large as 29. For most of accretion problems with  $v_r \ll v_\phi$ ,  $\delta$  is of order unity.

## 4. CODE VERIFICATION

We have verified our numerical algorithm by comparing our numerical results to a number of test problems with analytical solutions. These problems are designed to test the implementation of the different terms in the equations, such as the ones that describe gravity, pressure, and viscosity. In this section, we describe these tests in details <sup>2</sup>.

### 4.1. Free Fall of a Dust Ring

As a first test, we study the free-fall of an axisymmetric distribution of matter with no angular momentum, pressure, or viscosity. This problem tests the implementation of gravity, the radial boundary conditions, and the conservation of mass

<sup>2</sup> The simulation corresponding to these test can be find in the webpage <http://www.physics.arizona.edu/~chan/research/astro-ph/0406073/>.

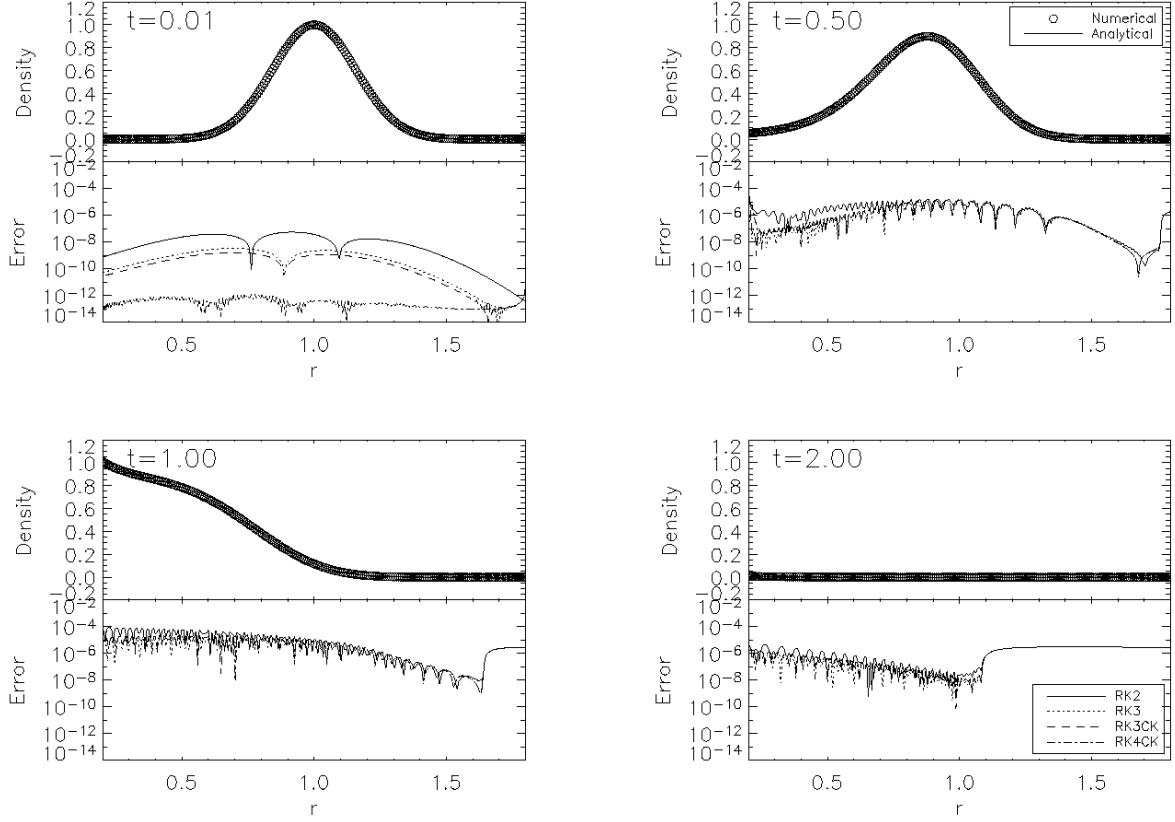


FIG. 2.— For each panel: (Top) The analytical solution (solid line) is compared to the numerical solution obtained with a third order Runge-Kutta (RK3) method (open circles). (Bottom) The numerical errors, defined as  $|\Sigma_{\text{num}} - \Sigma_{\text{ana}}|$ , at different times for the free-falling Gaussian ring discussed in §4.1. Different lines corresponds to different time-stepping schemes. The legend is in the bottom right plot.

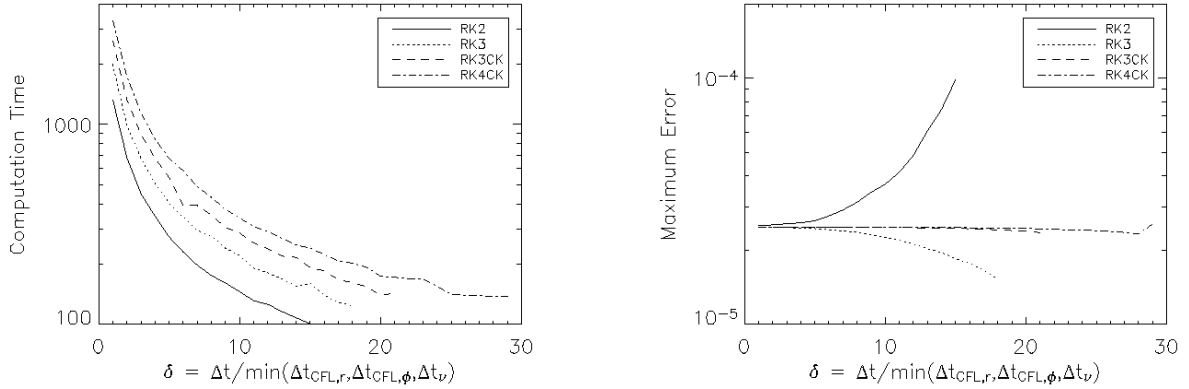


FIG. 3.— (Left) The vertical axis shows the computation time in seconds for the free-falling Gaussian ring problem (see §4.1), with different time stepping schemes. (Right) The vertical axis shows the numerical errors in the density profile for the same problem. The errors in the plot are the maximum of  $|\Sigma_{\text{num}} - \Sigma_{\text{ana}}|$  at  $t = 1$ . The horizontal axis for both plots are the dimensionless time stepping factor  $\delta = \Delta t / \min(\Delta t_{\text{CFL},r}, \Delta t_{\text{CFL},\phi}, \Delta t_{\nu})$  (see §3.6).

in the radial direction. Also, we use this problem to evaluate the efficiency and stability of the different time-stepping schemes. We set  $v_{\phi} = 0$ ,  $P = 0$ ,  $\nu_s = 0$ , and consider only Newtonian gravity with  $\mathbf{g} = (GM/r^2)\hat{\mathbf{r}}$ .

In order to verify our numerical result, we also solve the problem analytically. Using dimensionless quantities so that  $GM = 1$ , we write the conservation of energy for a fluid ele-

ment initially at  $r_0$  as

$$\left(\frac{dr}{dt}\right)^2 = \frac{2}{r} - \frac{2}{r_0}. \quad (54)$$

Integrating over time, we obtain the trajectory  $r = r(t; r_0)$  of each fluid element in the implicit form

$$\frac{\sqrt{2}}{r_0^{3/2}} t = \frac{1}{2} \sin \left( 2 \arccos \sqrt{\frac{r}{r_0}} \right) + \arccos \sqrt{\frac{r}{r_0}}. \quad (55)$$

We now consider conservation of mass, i.e., at any time we require that

$$2\pi r \Sigma(r, t) dr = 2\pi r_0 \Sigma_0(r_0) dr_0. \quad (56)$$

Evaluating  $dr_0$  by using equation (55), i.e.,

$$dr_0 = \frac{r_0 dr}{\sqrt{r_0/r - 1}} \left[ \frac{3}{2} \sqrt{\frac{2}{r_0}} t + \frac{r}{\sqrt{r_0/r - 1}} \right]^{-1}, \quad (57)$$

the analytical solution for the density becomes

$$\Sigma(r, t) = \Sigma_0(r_0) \frac{r_0^2}{r} \left[ \frac{3t}{2} \sqrt{\left(\frac{2}{r_0}\right) \left(\frac{r_0}{r} - 1\right) + r} \right]^{-1}, \quad (58)$$

where  $r_0$  can be obtained implicitly using equation (55).

Although this is an one dimensional problem, we simulate it in the two-dimensional domain  $[0.2, 1.8] \times [-\pi, \pi]$  with  $257 \times 64$  collocation points. The initial condition is a Gaussian ring

$$\Sigma_0(r, \phi) = \exp[-20(r-1)^2] \quad (59)$$

with zero initial velocity. At the outer boundary, we use the standard Neumann boundary conditions, i.e., we set  $(\partial \Sigma / \partial r)|_{r_{\text{out}}} = 0$  and  $(\partial v_r / \partial r)|_{r_{\text{out}}} = 0$  for all times. Moreover, because the characteristics at the inner boundary point towards the negative  $r$ -direction and we have neglected viscosity and pressure, we do not need to impose any explicit boundary conditions there. Because filtering stabilizes the flow, we do not apply any filters in this test in order to compare how different time-stepping methods affect the stability of the algorithm.

The top panels of Figure 2 compare the results of the simulations to the analytical solutions; the open circles denote the numerical results using the third order Runge-Kutta method and the solid lines are the analytical solution. The numerical results are indistinguishable from the analytical solution. The bottom panels of Figure 2 show the error between the numerical and analytical solution for the maximum stable time step.

We test four different time-stepping schemes: second order Runge-Kutta (RK2), third order Runge-Kutta (RK3), third order Carpenter-Kennedy (RK3CK), and four order Carpenter-Kennedy (RK4CK). Figure 3 shows the result of this test. In the left plot, the vertical axis shows the computation time. The horizontal axis shows the dimensionless time-stepping factor  $\delta = \Delta t / \min(\Delta t_{\text{CFL}, r}, \Delta t_{\text{CFL}, \phi}, \Delta t_{\nu})$  (see §3.6). The right plot shows the numerical errors,  $\max(|\Sigma_{\text{num}} - \Sigma_{\text{ana}}|)$ , at  $t = 1$ , for the same problem. For  $\delta > 15$  in RK2,  $\delta > 18$  in RK3,  $\delta > 21$  in RK3CK, and  $\delta > 29$  in RK4CK, the solutions diverge so neither the computation time nor the error are plotted in the graphs. This test demonstrates the ability of our algorithm to conserve mass to an accuracy better than a few parts in a million. It also demonstrates the advantage of the third order Runge-Kutta method over other algorithms, when solutions of high accuracy are necessary.

#### 4.2. Rayleigh's Criterion

We now study the ability of our algorithm to model correctly instabilities in hydrodynamic flows. In the absence of viscosity, the necessary and sufficient condition for a rotating flow with angular velocity  $\Omega(r)$  to be stable is

$$\frac{d}{dr}(r^2 \Omega)^2 > 0, \quad (60)$$

which is known as Rayleigh's criterion (Chandrasekhar 1981). Although Rayleigh's criterion usually describes the

TABLE 1  
NUMERICAL SOUND SPEEDS FOR THE PROBLEM DISCUSSED IN §4.4.

$\Gamma$	Numeric Sound Speed	Analytical Sound Speed	Percentage Error
1.0	1.011210	1.000000	1.12095%
1.1	1.062727	1.048808	1.32702%
1.2	1.107763	1.095445	1.12449%
1.3	1.153139	1.140175	1.13695%
1.4	1.193408	1.183216	0.86140%
1.5	1.235294	1.224744	0.86136%

stability condition in a Couette flow, i.e., for an incompressible fluid between two rotating cylinders, the criterion is also valid for rotating compressible fluids, when the unperturbed radial velocity vanishes everywhere in the flow. This can be achieved by balancing the centrifugal and centripetal accelerations. Let

$$\kappa^2 = 2\Omega \left( 2\Omega + r \frac{d\Omega}{dr} \right) \quad (61)$$

be the square of the epicyclic frequency. Rayleigh's criterion is equivalent to requiring  $\kappa^2 > 0$ , because  $d(r^2 \Omega)^2 / dr = r^3 \kappa^2$ .

We define a modified Newtonian gravity with a negative gravitational index  $\alpha < 0$  such that the gravitational acceleration is

$$g_r(r) \equiv -\frac{GM}{r^{|\alpha|}}. \quad (62)$$

Setting  $GM = 1$ , the corresponding ‘‘Keplerian’’ velocity  $v_\phi$  is given by

$$v_\phi = \sqrt{r^{\alpha+1}}. \quad (63)$$

Substituting this into Rayleigh's criterion, i.e., equation (60), we find that  $\alpha = -3$  is the critical stability condition. The growth rate of the instability is

$$\tau = \text{Im} \sqrt{\kappa^2} = \text{Im} \sqrt{(\alpha+3)r^{\alpha-1}}. \quad (64)$$

Of course, the same result can be obtained by observing that the effective potential

$$V_{\text{eff}}(r) = \frac{L^2}{2r^2} + \frac{1}{(\alpha+1)} r^{\alpha+1}, \quad (65)$$

has no local minimum when  $\alpha < -3$ ; here  $L$  is the angular momentum of a fluid element with a unit mass.

We use a spatial resolution of  $257 \times 64$  collocation points to test the Rayleigh criterion. The initial conditions are with a uniform density,  $\Sigma_0 = 1$ , and the velocity profile (63). Random perturbations that are of order  $10^{-6}$  are added to all physical quantities and the boundary conditions are set to  $v_r|_{r_{\text{min}}} = v_r|_{r_{\text{max}}} = 0$ .

Because Rayleigh's criterion refers to an one-dimensional problem, we discuss here explicitly the evolution of the  $m = 0$  mode. This is equivalent to averaging over the azimuthal direction. Figure 4 shows the evolution of power at  $k = 16, 32, 64$ , and  $128$  (and  $m = 0$ ) of the density, i.e., it is the plot of  $|\tilde{\Sigma}_{k,m}(t)|^2$  against time. When the flow is unstable, the perturbations grow very fast and diverge. As required by Rayleigh's criterion, flows with  $\alpha > -3$  are stable to perturbations.

#### 4.3. Propagation of Wavefronts

In order to test our implementation of the thermal pressure and the numerical spreading of wavefronts, we neglect gravity, set all velocities equal to zero, and simulate the propagation of a sound wave. We use the equation of state  $P = K \Sigma^\Gamma$



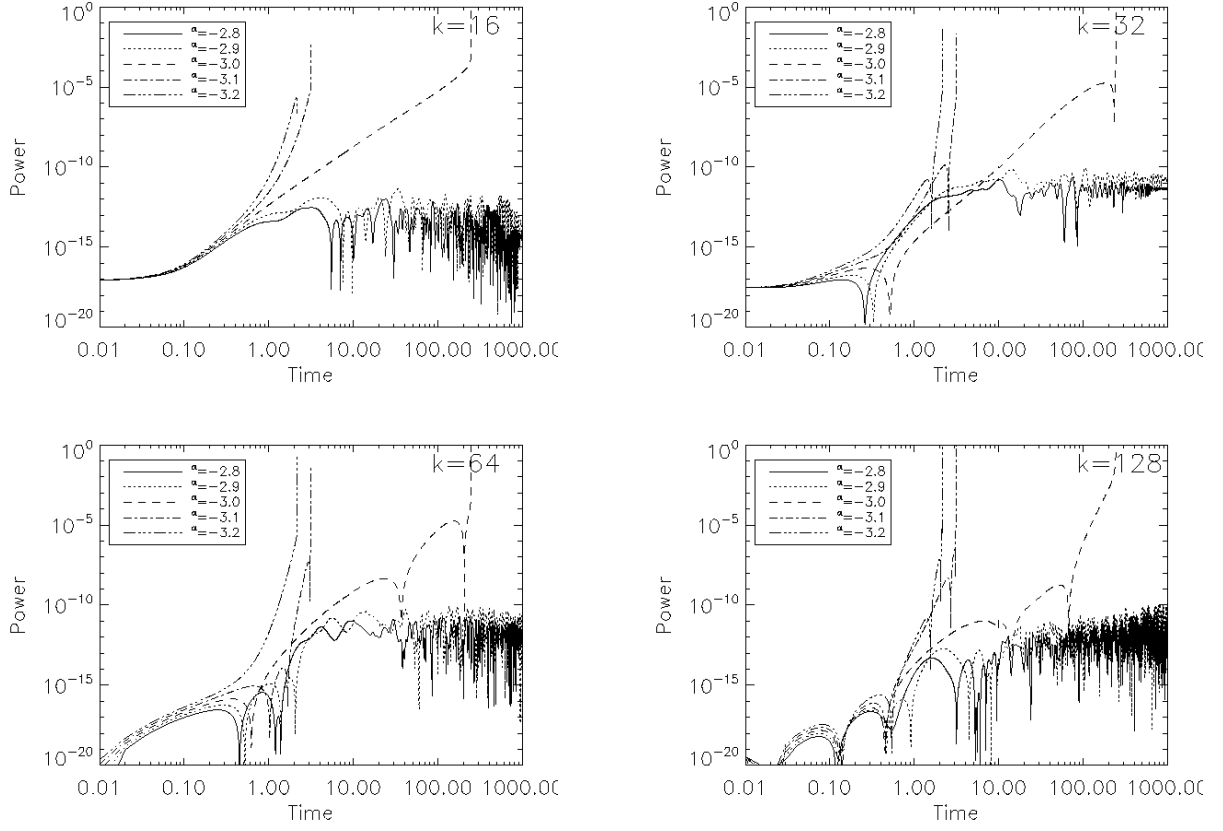


FIG. 4.— The evolution of the power at modes with  $k = 16, 32, 64$ , and  $128$  (and  $m = 0$ ) of the density for the study of Rayleigh's criterion discussed in §4.2.

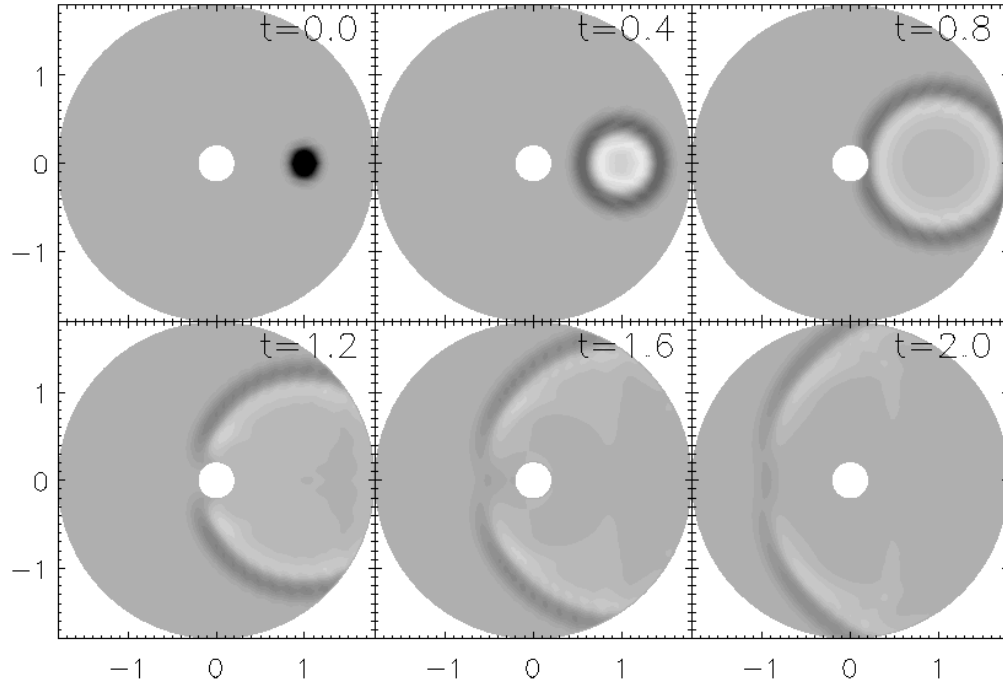


FIG. 5.— The propagation of a sound wave in a uniform static background. The gray-scale snapshots correspond to the fluid density; dark is high and light is low density.

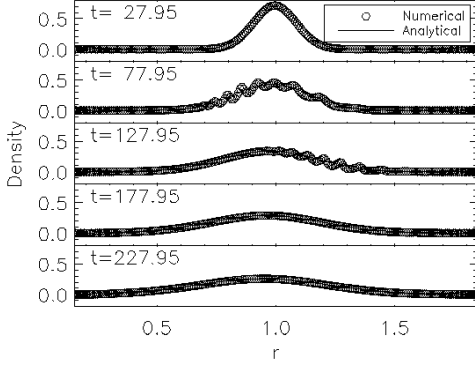


FIG. 6.— The evolution of a viscous spreading ring. The solid line is the analytical solution and the circles are numerical solutions. Note that concentric rings appear at the beginning, but, after about 24 ring rotations, they decay away and we recover the analytic solution.

with  $K = 1$  and vary the polytropic index  $\Gamma$  from 1 to 1.5. This pressure term decouples the energy equation from the Navier-Stokes equation and the sound speed is simply  $\sqrt{K\Gamma\Sigma^{\Gamma-1}}$ . The initial density is

$$\Sigma_0(r, \phi) = 1 + 10^{-6} \exp[-60(1 + r^2 - 2r \cos \phi)]. \quad (66)$$

We use  $257 \times 64$  collocation points and calculate the solution from  $t = 0$  to 2.

Figure 5 shows six gray-scale snapshots of the density for  $\Gamma = 1$ . The resulting sound wave propagates outward as a circle. Note that, because of our boundary treatment, the density wave is not reflected back as it propagates close to the boundaries. To measure the sound speed, we take the density profile at  $\phi = 0$  and trace the wavefronts. The collocation points that correspond to the peak density are then used to calculate, via  $\chi^2$ -fitting, the sound speed. Table 1 shows the  $\chi^2$ -fitted sound speed of the simulation. Compared to the analytical sound speed, the error is of order 1%.

#### 4.4. Viscous Spreading of a Fluid Ring

The spreading of an axisymmetric viscous ring with small kinematic viscosity  $\nu_s$  (Pringle 1981; Frank, King, & Raine 2002) has become a standard test for numerical methods including both smoothed particle hydrodynamics (SPH) and grid-based codes. It has also often been used to guide studies of many other astrophysical problems, such as the fall-back disk after a supernova explosion (see, e.g., van Paradijs et al. 1995; Ekşi, & Alpar 2003).

In the standard solution, it is assumed that  $v_\phi = r\Omega_K \gg v_r$ , so the viscosity tensor can be approximated by

$$\tau_{rr} = \tau_{\phi\phi} = 0, \quad \tau_{r\phi} = \tau_{\phi r} = \nu_s \Sigma \left( \frac{\partial v_\phi}{\partial r} - \frac{v_\phi}{r} \right). \quad (67)$$

Using conservation of mass, conservation of angular momentum, the fact that  $v_\phi$  is always close to the Keplerian value, and assuming that the kinematic viscosity coefficient  $\nu_s$  is a constant, the analytical solution for the density, in our units, becomes

$$\Sigma(r, t) = \frac{1}{12\pi\nu_s r^{1/4} t} \exp\left(-\frac{1+r^2}{12\nu_s t}\right) I_{1/4}\left(\frac{2r}{12\nu_s t}\right), \quad (68)$$

where  $I_{1/4}$  is a modified Bessel function.

We perform our simulations with axisymmetric initial conditions. We follow Speith, & Kley (2003) and use a typical value  $\nu_s = 4.77 \times 10^{-5}$ . The energy equation is decoupled from the hydrodynamic equations as in the previous subsection. We set  $\Gamma = 1$ , and choose  $K$  such that  $c_s = 10^{-8}$ . The spatial resolution is  $257 \times 64$  and the time step factor  $\delta = 0.8$ . We start with an initial density given by equation (68) at  $t = 27.95$ , which corresponds to  $12\nu_s t = 0.016$ . The boundary conditions are  $v_\phi|_{r_{\max}} = (r\Omega_K)|_{r_{\max}}$  and  $v_\phi|_{r_{\min}} = (r\Omega_K)|_{r_{\min}}$ , which are the ones assumed in the standard solution.

Figure 6 compares the analytical solution to the numerical solution. The simulation shows that some concentric rings appear at the beginning. They come from the relaxation effect as our initial velocities approach standard solution. In fact, these additional structures have been found in other simulations (for more information see Monaghan 1992), and decay away after about 24 rotations.

#### 4.5. Shakura-Sunyaev Steady Disk Solution

Here we consider the thin disk problem and suppose that the disk is able to settle to a steady-state structure. By assuming an  $\alpha$ -viscosity law, Shakura, & Sunyaev (1973) solved the local disk structure analytically. Their work has been highly cited for studies in accretion disks. (See Frank, King, & Raine 2002 and reference therein).

In our simulation, we solve the hydrodynamic equations (1) – (3) including the energy equation. The kinematic viscosity coefficient is given by

$$\nu_s = \alpha c_s H. \quad (69)$$

The sound speed is given by  $c_s^2 = \partial P / \partial \Sigma = k_B T / \mu m_H$  and the disk scale height is  $H = rc_s / v_\phi$ . We, also, assume the vertical optical depth of the disk to be  $\tau_d = \Sigma \kappa_R$ , where the Rosseland mean opacity  $\kappa_R$  is given by Kramer's law<sup>3</sup>

$$\kappa_R = 6.07 \times 10^{22} \frac{\Sigma}{\sqrt{4\pi H}} T^{-7/2} \text{cm}^2 \text{g}^{-1}, \quad (70)$$

Based on the above assumption and using the fact that  $\nu_s$  is small, the Shakura-Sunyaev disk solution is given by

$$\Sigma = 6.15 \alpha^{-4/5} \dot{M}_{16}^{7/10} m_1^{1/4} R_{10}^{-3/4} f^{14/5} \text{g cm}^{-2}, \quad (71)$$

$$v_r = -2.59 \times 10^4 \alpha^{4/5} \dot{M}_{16}^{3/10} m_1^{-1/4} R_{10}^{-1/4} f^{-14/5} \text{cm s}^{-1}, \quad (72)$$

$$v_\phi = 1.15 \times 10^8 m_1^{1/2} R_{10}^{-1/2} \text{cm s}^{-1}, \quad (73)$$

$$T = 1.48 \times 10^4 \alpha^{-1/5} \dot{M}_{16}^{3/10} m_1^{1/4} R_{10}^{-3/4} f^{6/5} \text{K}, \quad (74)$$

where  $\dot{M}_{16} = \dot{M} / 10^{16} \text{g s}^{-1}$ ,  $m_1 = M / M_\odot$ ,  $R_{10} = r / (10^{10} \text{cm})$ , and  $f = (1 - \sqrt{R_*/r})^{1/4}$ , with  $R_*$  being the radius of the central object. Considering the flow around a standard neutron star with a mass of  $1.4M_\odot$ , and a radius of  $8.5 \times 10^5 \text{cm}$ , we setup the simulation with  $r_{\min} = 10^9 \text{cm}$  and  $r_{\max} = 1.2 \times 10^{11} \text{cm}$ . The initial conditions for density and energy are as the Shakura-Sunyaev disk solution with  $\dot{M}_{16} = 1$ ,  $m_1 = 1.4$ , and  $\alpha = 0.1$ . We set the initial radial velocity to zero and the initial azimuthal velocity to be Keplerian. Perturbations were added to all variables with amplitude 0.1 and order 3. The simulation runs with  $513 \times 64$  collocation points up to  $t = 10^7 \text{s}$ , which is approximately 16 viscous time scales.

In Figure 7, we show our numerical steady solution for  $\alpha = 0.1$ , at  $t = 10^7 \text{s}$ ; note that we use the magnitude of the

<sup>3</sup> See again Frank, King, & Raine (2002), p.94 for notes on errors in the literature.

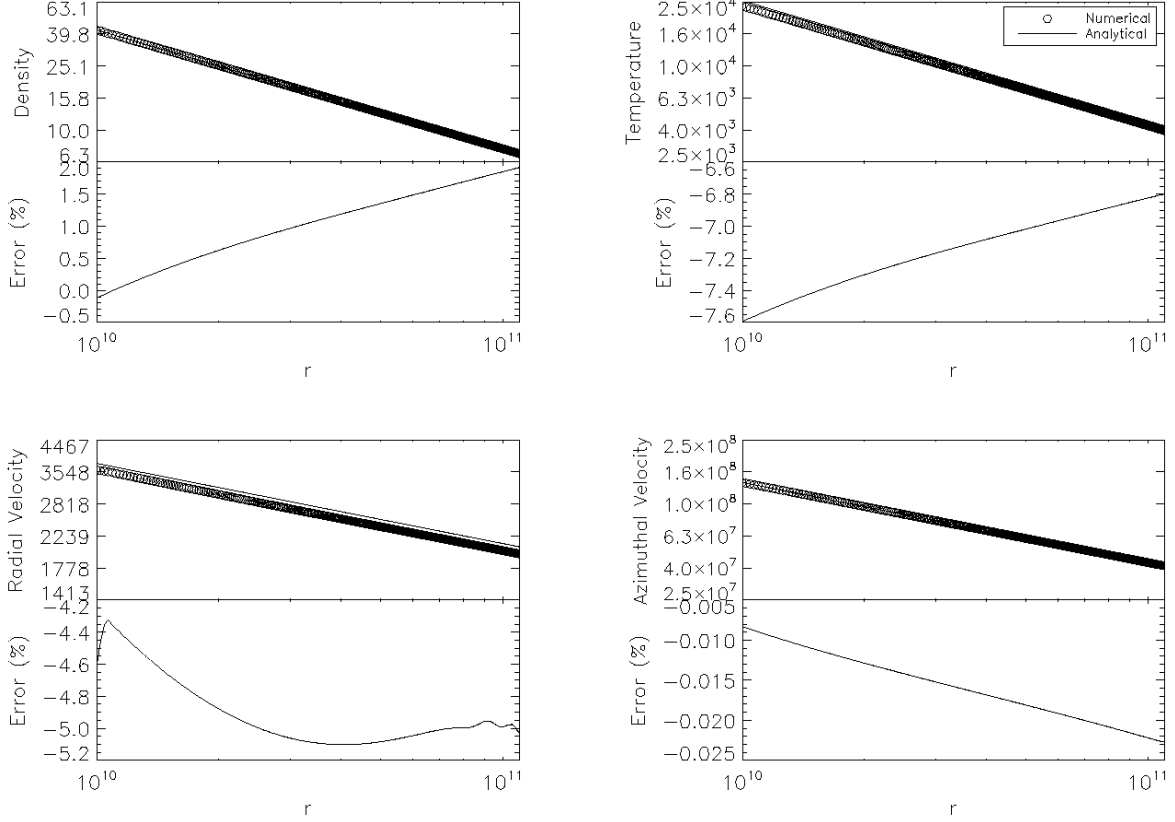


FIG. 7.—(Top) The analytical solution (solid line) compared to the numerical solution (open circles) of the Shakura-Sunyaev steady disk solution in log-log scale. (Bottom) The percentage numerical errors, defined as  $(f_{\text{num}}/f_{\text{ana}} - 1) \times 100\%$ . All the units along the vertical axis are cgs units, i.e.,  $\text{g cm}^{-2}$  for density, K for temperature, and  $\text{cm s}^{-1}$  for velocities.

radial velocity in order to plot it in log-log scale. The numerical values are different from the Shakura-Sunyaev solution by a few percent. We point out explicitly that the pressure term in the Navier-Stokes equation is neglected in obtaining the analytical solution. Although the pressure does not transport angular momentum, the effect of pressure compared to those of viscosity is proportional to  $1/\alpha$ . Since  $\alpha = 0.1$  in our simulation, the pressure effects can account for the difference between the analytical and numerical solution.

##### 5. APPLICATION: NON-AXISYMMETRIC INSTABILITIES IN VISCOUS SPREADING RINGS

As we mentioned in §4.4, the viscous spreading ring has become a standard test for numerical simulations. In these simulations, additional structures always appear, such as the concentric rings in Figure 6. We attributed the presence of these concentric rings to relaxation effects of the initial conditions. Maddison et al. (1996), on the other hand, showed that the concentric rings that appear in SPH simulations using the artificial viscosity given by Monaghan (1992) are numerical artifacts. Later, Speith, & Kley (2003) used perturbation methods to show that viscous spreading rings are unstable to non-axisymmetric perturbations.

Assuming a compressible, pressureless, and viscous fluid, the equations used in Speith, & Kley (2003) are the continuity equation (1) and the Navier-Stokes equation (2), with zero pressure. By setting  $\nu_s = \mu_s/\Sigma$  to be constant and  $\mu_r = \mu_b = 0$ , the first order instability is an one-armed spiral, whereas

the second order instability is a superposition of an one-armed and a two-armed spirals.

If we define a function

$$\hat{E}(t, r) = 2 - \frac{2\nu_\phi}{r\Omega_K}, \quad (75)$$

where  $\Omega_K = \sqrt{GM/r^3}$  is the Keplerian angular velocity, then  $\hat{E}(t, r)$  measures the first order perturbation amplitude. Its dispersion relation is

$$\sigma_d = -k \left( \frac{\nu_s}{r} + \frac{8}{3} \frac{\nu_s}{\hat{\Sigma}_0} \frac{\partial \hat{\Sigma}_0}{\partial r} \right) + i \left( k^2 \frac{\nu_s}{3} - \frac{\nu_s}{r\hat{\Sigma}_0} \frac{\partial \hat{\Sigma}_0}{\partial r} \right) \quad (76)$$

where  $k$  is the radial wavenumber and  $\hat{\Sigma}_0$  is the standard solution (68). Assuming  $12\nu_{st} \ll r$ , it follows that the condition for instability is

$$k^2 > \frac{3}{r\hat{\Sigma}_0} \frac{\partial \hat{\Sigma}_0}{\partial r} \quad (77)$$

and the growth rate is

$$\text{Im}(\sigma_d) = \frac{1}{3} k^2 \nu_s + \frac{3\nu_s}{4r^2} + \frac{1}{6t} (1-r). \quad (78)$$

In order to test this claim, we carried out a test with the same condition as Speith and Kley's RH2D simulation (a radiative hydrodynamic code; see Kley 1989). The only differences are in the initial perturbations and a small constant background term in the density, i.e., the setup is the same as in §4.4 but

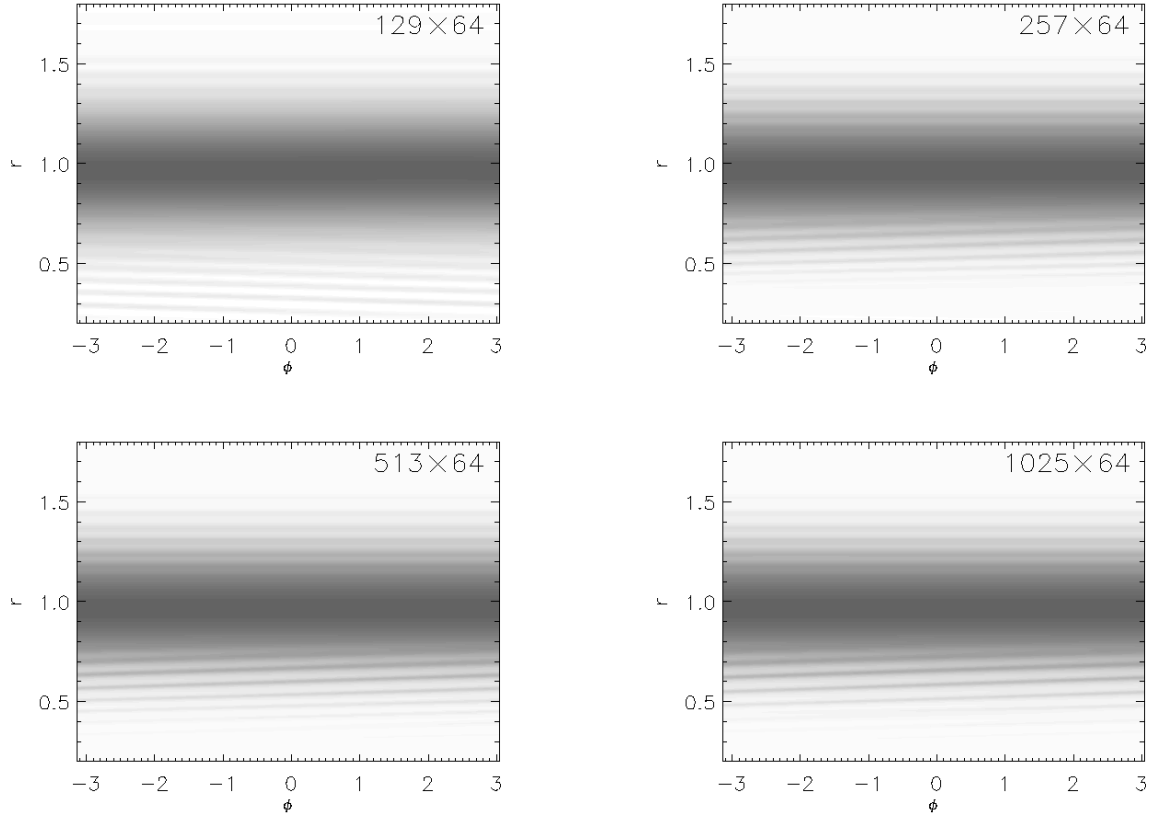


FIG. 8.— Snapshot of simulations of a viscous spreading ring with different resolutions. Note that for different resolution, the direction of the spirals are different.

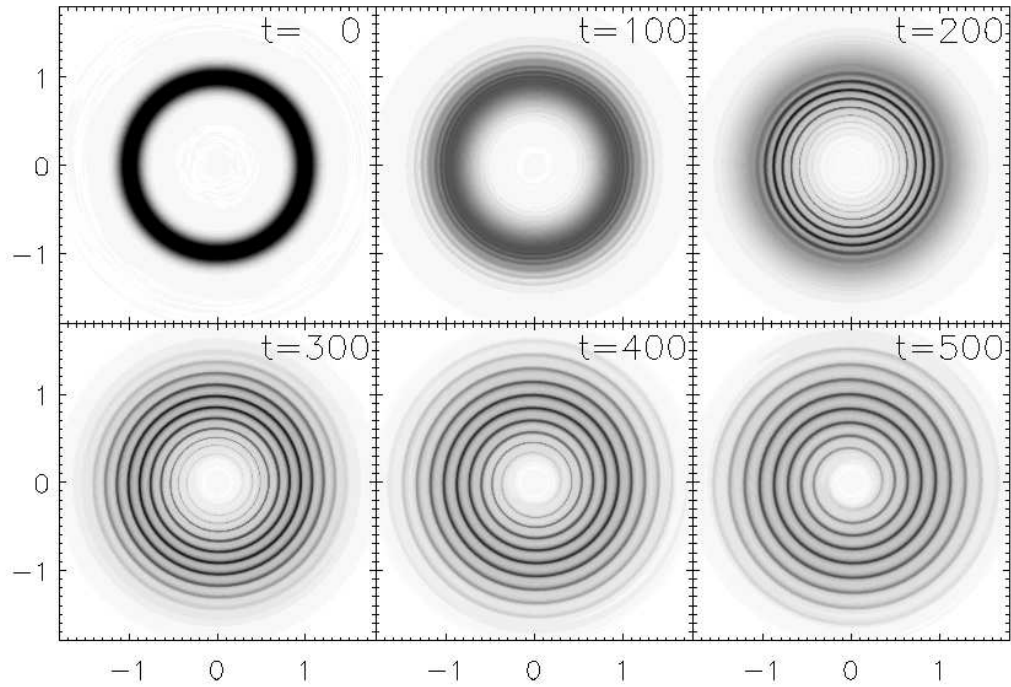


FIG. 9.— The evolution of a viscous spreading ring with non-axisymmetric perturbations. At  $t = 100$ , there are concentric rings due to the initial relaxation. At  $t = 200$  it is clear that a small, one-armed spiral starts to develop in the inner region. The remaining figures, then, show the development of the one-armed spiral.

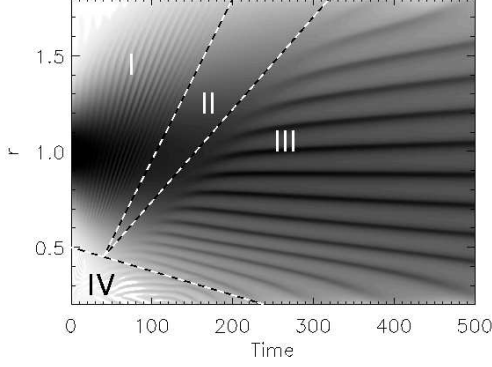


FIG. 10.— The contour plot of density at  $\phi = 0$  against time. Region I shows the relaxation effect. Region II shows that the solution has relaxed to the standard solution. The Speith-Kley instability develops in region III. In region IV, the unstable wavelengths are too short to be resolved in our numerical method.

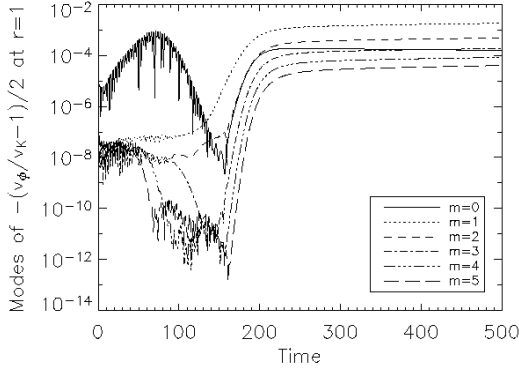


FIG. 11.— The evolution of the first 6 modes of  $\hat{E}(r=1, t)$ .

we add initial perturbations by the method described in §3.4 with order 3 and magnitude 0.001. The additional constant background term in the density varies from 0.1 to 0.001 depending upon the resolution, which keeps the solution stable. We perform the simulation with resolution  $129 \times 64$ ,  $257 \times 64$ ,  $513 \times 64$ , and  $1025 \times 64$ .

Figure 8 shows the density contours for different resolutions at time  $t = 120$ . It is clear that the direction of the spiral in low resolution is different then in high resolution. We confirm this result with Speith and Kley (private communication), i.e., that the transition radius between leading and trailing spirals vary as the resolution changes. Figure 9 is the density contour of the simulation with  $513 \times 64$  collocation points and 0.001 background density, at different times. At  $t = 100$ , some concentric rings due to relaxation effects are seen. At  $t = 200$ , a one-armed spiral starts to form at the inner disk. The spiral is fully developed by  $t = 300$ .

In order to find out the unstable wave number, we plot in Figure 10 the contour of density along  $\phi = 0$  against time. Region I shows the relaxation effect, where the relaxation waves propagate outwards. In region II, the solution has relaxed to the standard solution. Later on, the Speith-Kley instability starts to develop, which is shown in region III. We can estimate the wavelength of the fully developed spirals, which varies from 0.1 to 0.15. For region IV, the unstable wavelengths are too short to be resolved in our numerical method.

Finally, in Figure 11 we plot the first 6 modes, i.e.,  $m = 0, 1, \dots, 5$ , of  $\hat{E}(r=1, t)$ . The late time behavior of our solution agrees with Figure 8 in Speith, & Kley (2003). To compare our numerical result with the analytical growth rate (78), we  $\chi^2$ -fit the slope of the  $m = 1$  mode in Figure 11 between  $t = 250$  and  $t = 500$ , which gives  $\text{Im}(\sigma_d) \approx 0.0013$ . That corresponds to unstable wavenumber  $k \approx 9.0$ . It agrees with the width of the spiral  $\approx 0.11$  as shown in Figures 9 and 10.

Physically, the viscous spreading ring problem is an important guide to understanding the transport of angular momentum in accretion disks. We have independently verified the Speith-Kley instability: a cold viscous disk is unstable to non-axisymmetric perturbations.

## 6. CONCLUSIONS

We described a numerical method based on a pseudo-spectral algorithm for studying the rapid variability properties of two-dimensional, viscous, hydrodynamic accretion disks. We demonstrated the ability of the spectral methods to handle correctly non-reflective boundary conditions and different stability conditions. We verified the implementation of the algorithm using various test problems. Also, we confirmed the non-axisymmetric instability of viscous spreading rings discovered by Speith and Kley.

Spectral methods calculate the time evolution of a solution as an interaction of different waves. From a mathematical point of view, this approach naturally agrees with existing methods to study non-linear equations. It helps us to confirm directly the result of linear mode analysis as well as turbulence theories. From a computational point of view, these methods are high order and produce accurate result in most problems. It is straightforward to extend the current algorithm to simulate 3D MHD accretion disks. In particular, because of the high order of the spectral methods, we can solve directly for the vector potential and not for the magnetic field, in order to guarantee that the resulting field will be free of divergence at each time step. Also, spectral methods can be used to solve self-gravity problem without increasing significantly the computation time. Finally, and most important, from a physical point of view, our algorithm provides another tool to set up numerical experiments and test astrophysical models. It is useful to confirm independently the results from other numerical simulations as well as test new models.

## APPENDIX

### A. CONVECTION-CONSERVATIVE MIXED FORMULISM

As we describe in §3.2, we employ a convective-conservative mixed method. The non-linear term  $(\mathbf{v} \cdot \nabla)\mathbf{v}$  in the Euler equation is implemented in convective form, and all other terms are in conservation form.

$$\partial_t \Sigma = -\frac{\partial_r(r\Sigma v_r)}{r} - \frac{\partial_\phi(\Sigma v_\phi)}{r}, \quad (\text{A1})$$

$$\partial_t v_r = -v_r \partial_r v_r - \frac{v_\phi}{r} (\partial_\phi v_r - v_\phi) + \frac{\partial_r(r\tau_{rr} - rP)}{r\Sigma} + \frac{\partial_\phi \tau_{r\phi}}{r\Sigma} + \frac{P - \tau_{\phi\phi}}{r\Sigma} - g_r, \quad (\text{A2})$$

$$\partial_t v_\phi = -v_r \partial_r v_\phi - \frac{v_\phi}{r} (\partial_\phi v_\phi + v_r) + \frac{\partial_r(r\tau_{r\phi})}{r\Sigma} + \frac{\partial_\phi(\tau_{\phi\phi} - P)}{r\Sigma} + \frac{\tau_{r\phi}}{r\Sigma}, \quad (\text{A3})$$

$$\partial_t E = -\frac{\partial_r(rEv_r + rq_r + rF_r)}{r} - \frac{\partial_\phi(Ev_\phi + q_\phi + F_\phi)}{r} - P \left( \partial_r v_r + \frac{\partial_\phi v_\phi}{r} + \frac{v_r}{r} \right) + \phi - 2F_z. \quad (\text{A4})$$

Here, the notation  $\partial_t$  denote partial derivative with respect to time. The other notations  $\partial_r$  and  $\partial_\phi$  denote the numerical derivative operators. Hence, the notation  $v_r \partial_r v_r$  means, we first take a numerical derivative of the variable  $v_r$  and multiply the result with  $v_r$ , which is in convective form. On the other hand,  $\partial_r(r\Sigma v_r)/r$  means, we first use a temporary variable to store the produce  $r\Sigma v_r$ , apply the procedure to calculate the numerical derivative on it, and then divide it by  $r$ . This is the conservative form.

The viscosity tensor  $\tau_{ij}$  in the above equation has the following general form

$$\tau_{ij} = 2(\mu_r + \mu_s)e_{ij} + \left( \mu_r + \mu_b - \frac{2}{3}\mu_s \right) \nabla \cdot \mathbf{v}. \quad (\text{A5})$$

As we describe before,  $\mu_r$ ,  $\mu_b$ , and  $\mu_s$  are coefficient of radiative, bulk, and shearing viscosity. The strain rate tensor  $e_{ij}$  written in cylindrical coordinate becomes

$$e_{rr} = \partial_r v_r \quad (\text{A6})$$

$$e_{r\phi} = e_{\phi r} = \frac{1}{2} \left( \partial_r v_\phi - \frac{v_\phi}{r} + \frac{\partial_\phi v_r}{r} \right) \quad (\text{A7})$$

$$e_{\phi\phi} = \frac{\partial_\phi v_\phi}{r} + \frac{v_r}{r} \quad (\text{A8})$$

and  $\nabla \cdot \mathbf{v}$  in cylindrical coordinate is

$$\nabla \cdot \mathbf{v} = \partial_r v_r + \frac{v_r}{r} + \frac{\partial_\phi v_\phi}{r}. \quad (\text{A9})$$

For completeness, we provide again the viscous dissipation rate

$$\phi = 2(\mu_r + \mu_s)(e_{ij})^2 + \left( \mu_r + \mu_b - \frac{2}{3}\mu_s \right) (\nabla \cdot \mathbf{v})^2. \quad (\text{A10})$$

The functional forms of  $P$ ,  $\mu_r$ ,  $\mu_b$ ,  $\mu_s$ ,  $\mathbf{q}$ ,  $\mathbf{F}$ , and  $F_z$  can be change easily depend upon the physical assumption (where the defaults are described in §2).

C.-K. C. and D. P. acknowledge the support from a NASA ATP grant NAG-513374. F. Ö. acknowledges support by NASA through Hubble Fellowship grant HF-01156 from the Space Telescope Science Institute, which is operated by the Association of Universities for Research in Astronomy, Inc., under NASA contract NAS 5-26555.

#### REFERENCES

- Abramowicz, M.A., & Kluźniak, W. 2001, *A&A*, 374, L19  
 Armitage, P.J., & Reynolds, C.S. 2003, *MNRAS*, 341, 1041  
 Bonazzola, S., Gourgoulhon, E., & Marck, J.-A. 1999, *J. Comp. Appl. Math.* 109, 433  
 Botella, O., & Peyret, R. 2001, *Int. J. Numer. Methods Fluids*, 36, 125  
 Boyd, J.P. 2000, *Chebyshev and Fourier Spectral Methods*, 2nd Edition (New York: Dover)  
 Canuto, C., Hussaini, M.Y., Quarteroni, A., & Zang, T.A. 1988, *Spectral Methods in Fluid Dynamics* (New York: Springer)  
 Chandrasekhar, C. 1981, *Hydrodynamic and Hydromagnetic Stability* (New York: Dover)  
 Chen, H., Su, Y., & Shizgal, B.D. 2000, *J. of Comp. Phys.* 160, 453  
 Chen, X., & Taam, R.E. 1994, *ApJ*, 431, 732  
 ———. 1995, *ApJ*, 441, 354  
 Don, W.S. 1994, *J. of Comp. Phys.* 110, 103  
 Don, W.S., & Quillen, C.B. 1995, *J. of Comp. Phys.* 122, 244  
 Don, W.S., & Solomonoff, A. 1997, *SIAM J. Scien. Comp.* 18, no. 4, 1040  
 Ekşi, K.Y., & Alpar, M.A. 2003, *ApJ*, 599, 450  
 Frank, J., King, A., & Raine, D. 2002, *Accretion power in astrophysics* (Cambridge University Press)  
 Gammie, C.F., & Balus, S.A. 1994, *MNRAS*, 270, 138  
 Godon, P. 1997, *ApJ*, 480, 329  
 Godon, P. 1998, *ApJ*, 502, 382  
 Godon, P., & Livio, M. 1997, *ApJ*, 537, 396  
 Gottlieb, D., & Orszag, S.A. 1983, *Numerical Analysis of Spectral Methods: Theory and Applications* (Philadelphia: SIAM)  
 Gottlieb, D., & Shu, C.-W. 1983, *SIAM Rev.* Vol. 39, No. 4, 644  
 Guo, B.Y. 1998, *Spectral Methods and Their Applications* (Singapore: World Scientific)  
 Guo, B.Y., Ma, H.P., Tadmor, E. 2001, *SIAM J. Numer. Anal.* 39, No. 4, 12254  
 Hawley, J. F. & Krolik, J. H. 2001, *ApJ*, 548, 348  
 ———. 2002, *ApJ*, 566, 164  
 Hubeny, I. 1990, *ApJ*, 351, 632  
 Kato, S. 2001, *PASJ*, 53, 1  
 Kley, W. 1989, *A&A*, 208, 98  
 Kosloff, D., & Tal-Ezer, H. 1993, *J. Comp. Phys.* 104, 457  
 LeVeque, R.J. 1992, *Numerical Methods for Conservation Laws* (Basel: Birkhäuser)  
 Li, H. 2001, *Super Spectral Viscosity Methods for Nonlinear Conservation Laws, Chebyshev Collocation Methods and Their Applications* (Thesis)  
 Ma, H. 1998, *SIAM J. Numer. Anal.* Vol. 35, No. 3, 869  
 Ma, H. 1998, *SIAM J. Numer. Anal.* Vol. 35, No. 3, 893  
 Maddison, S.T., Murray, J.R., & Monaghan, J.J. 1996, *Publ. Astron. Soc. Aust.* 13, 66  
 McClintock, J.E., & Remillard R.A. 2004, in *Compact Stellar X-ray Sources*, eds. W.H.G. Lewin and M. van der Klis (Cambridge: University Press)  
 Menou, K. 2003, *ApJ*, 596, 414  
 Monaghan, J.J. 1992, *ARA&A*, 30, 534  
 Mote, P.W., & O'Neill, A. 2000, *Numerical modeling of the global atmosphere in the climate system* (Dordrecht; Boston: Kluwer Academic)  
 Milsom, J.A., & Taam, R.E. 1996, *MNRAS*, 283, 919  
 ———. 1997, *MNRAS*, 286, 358  
 Mukhopadhyay, B. 2002, *Apj*, 581, 427

- Paczynski, B., & Wiita, P.J. 1980, A&A, 88, 23
- Peyret, R. 2002, *Spectral Methods for Incompressible Viscous Flow* (New York: Springer)
- Popham, R. & Narayan, R. 1995, Apj, 442, 337
- Pringle, J.E. 1981, ARA&A, 19, 137
- Psaltis, D. 2001, Adv. Sp. Res., 24, 481
- . 2004, in *X-ray Timing 2003: Rossi and Beyond*, eds. P. Kaaret, F.K. Lamb, and J.H. Swank
- Rezzolla, L. 2004, in *X-ray Timing 2003: Rossi and Beyond*, eds. P. Kaaret, F.K. Lamb, and J.H. Swank
- Shakura, N.I., & Sunyaev, R.A. 1973, A&A, 24, 337
- Speith, R., & Kley, W. 2003, A&A, 399, 395
- Strohmayer, T.E. 2001a, ApJ, 554, L169
- . 2001b, ApJ, 552, L49
- van der Klis, M. 2000, ARA&A, 38, 717
- van Paradijs, J., Taam, R.E., & van den Heuvel, E.P.J. 1995, A&A, 299, L41
- Wagoner, R.V. 1999, Physics Reports, 311, 259
- Wagoner, R.V., Silbergleit, A.S., & Ortega-Rodriguez, M. 2001, ApJ, 559, L25